

RESEARCH ARTICLE

10.1002/2016JC012573

The evolution of scaling laws in the sea ice floe size distribution

Christopher Horvat¹  and Eli Tziperman¹ ¹Department of Earth and Planetary Sciences and School of Engineering and Applied Sciences, Harvard University, Cambridge, Massachusetts, USA

Key Points:

- Scaling behavior of the sea ice floe size distribution due to floe-scale processes is analyzed
- Relationships between steady-state power-law scaling and physical processes are described and identified
- Sources of biases in sea ice simulations due to assumed power-law behaviors are diagnosed and examined

Supporting Information:

- Supporting Information S1

Correspondence to:

C. Horvat,
horvat@fas.harvard.edu

Citation:

Horvat, C., and E. Tziperman (2017), The evolution of scaling laws in the sea ice floe size distribution, *J. Geophys. Res. Oceans*, 122, 7630–7650, doi:10.1002/2016JC012573.

Received 22 NOV 2016

Accepted 26 JUN 2017

Accepted article online 5 JUL 2017

Published online 21 SEP 2017

Abstract The sub-gridscale floe size and thickness distribution (FSTD) is an emerging climate variable, playing a leading-order role in the coupling between sea ice, the ocean, and the atmosphere. The FSTD, however, is difficult to measure given the vast range of horizontal scales of individual floes, leading to the common use of power-law scaling to describe it. The evolution of a coupled mixed-layer-FSTD model of a typical marginal ice zone is explicitly simulated here, to develop a deeper understanding of how processes active at the floe scale may or may not lead to scaling laws in the floe size distribution. The time evolution of mean quantities obtained from the FSTD (sea ice concentration, mean thickness, volume) is complex even in simple scenarios, suggesting that these quantities, which affect climate feedbacks, should be carefully calculated in climate models. The emergence of FSTDs with multiple separate power-law regimes, as seen in observations, is found to be due to the combination of multiple scale-selective processes. Limitations in assuming a power-law FSTD are carefully analyzed, applying methods used in observations to FSTD model output. Two important sources of error are identified that may lead to model biases: one when observing an insufficiently small range of floe sizes, and one from the fact that floe-scale processes often do not produce power-law behavior. These two sources of error may easily lead to biases in mean quantities derived from the FSTD of greater than 100%, and therefore biases in modeled sea ice evolution.

Plain Language Summary Sea ice is an incredibly complex mosaic of individual pieces, known as floes, with sizes that range from centimeters to tens of kilometers. The precise distribution of these floes is an important factor in climate simulation, as it affects how the ice, ocean, and the atmosphere evolve together. Observing the full range of floe sizes is a serious technical challenge, and sea ice has long been assumed to have a fractal distribution of floe sizes, one that can be described by a power law. We address whether this assumption is sensible by explicitly simulating how floes respond to climate forcing, leading to floes that melt, collide, and fracture. We find that the distribution of floe sizes is often not a power law, and errors caused by assuming this sort of power law behavior can lead to significant errors in how sea ice is simulated. In some cases, power-law behavior is observed, like in long simulations when waves break ice floes that are colliding with one another. We highlight the need to observe and understand this incredibly rich and complex system in greater detail before making assumptions that will be incorporated into new climate models.

1. Introduction

Sea ice is a complex, multi-scale mosaic of floes with a wide variety of thicknesses, and with horizontal sizes that can range from centimeters to tens of kilometers, often below the grid scale of typical global climate models (GCMs). As the Arctic sea ice cover has declined and thinned in the recent past, it is more sensitive to fracture by ocean surface waves that break the ice into small floes. Parameterizing the evolution of the sub-gridscale distribution of floe sizes and its interaction with climate processes is therefore now an important objective for sea ice models. Yet very little is known about how the sub-gridscale distribution of floe size evolves, nor how the wide range of scaling laws typically ascribed to floe size measurements may emerge due to processes acting on individual floes. No current climate model simulates the evolution of the floe size distribution, nor parameterizes its influence on other aspects of the coupled climate system. This study focuses on understanding how climate forcing may determine the evolution of the sub-gridscale floe size and thickness distribution, and how scaling laws develop.

The sub-gridscale distribution of sea ice floes is described by the floe size and thickness distribution (FSTD), $f(r, h)$, with $f(r, h) dr dh = f(\mathbf{r}) d\mathbf{r}$ equal to the fraction of the ocean surface covered by floes with a size between r and $r + dr$ and a thickness between h and $h + dh$. The integral of f over all sizes r is the ice thickness distribution (ITD), the evolution of which is an important component of modern sea ice models [e.g., Bitz, 2008]. The integral of f over all thicknesses h is the floe size distribution (FSD). The FSD plays an important role in sea ice melting [Steele, 1992; Horvat et al., 2016], rheology [Feltham, 2008; Herman, 2012; Rynders et al., 2016], the propagation of ocean surface waves [Dumont et al., 2011; Bennetts and Williams, 2014], and the exchange of buoyancy and momentum in the ocean and atmospheric boundary layers [Birnbaum and Lüpkes, 2002; Tsamados et al., 2014]. Parameterizations of lateral melting and form drag sensitive to floe size have significant impact in climate model simulations [Tsamados et al., 2015], but cannot be evaluated properly as floe size is not a prognostic variable in any modern GCM.

Hampering efforts to parameterize the evolution of the FSD/FSTD for climate model simulations is the lack of detailed observations of the FSD and its evolution in the polar oceans. The FSD has been observed at isolated points in both space and time over the past four decades. From these observations, a consensus has developed that the FSTD decays as a power-law distribution in floe size. Yet observations of floe size distributions do not support the existence of a universal power law: for example, observed power-law-fit exponents span a very wide range, from as low as 0.91 [Steer et al., 2008] to 5 and greater [Toyota et al., 2011]. Both of these observations were made at the ice edge in the Weddell Sea. Most observational studies are inconsistent in whether they support of power law decay at all. Often, fitting to measurements is done over a narrow range of floe sizes. When the range of resolved floe sizes is expanded [i.e., Toyota et al., 2006, 2011], observations are fit to two power-laws covering different size ranges, with variable slopes. The observed distribution of floe sizes is indeed often better fit by non power-law distributions [Herman, 2011]. Examining the common hypothesis that the FSD is a self-similar (power law) distribution is a main objective of this study.

The observed wide variability and weak fit of power-law exponents to observations demonstrate our limited understanding of the evolution of the floe size distribution. We do not yet understand when and due to what processes power law behavior is to be expected. Of course, if power laws are observed, one wants to understand which of the physical processes that shape floes leads to the emergence of what types of power laws. As an explicit simulation of the FSD may not be practical in most climate studies, it is also important to understand the evolution of quantities such as the mean floe size and power-law slopes, for use in wave-ice interaction models [Williams et al., 2013] or floe-size-dependent rheologies [Rynders et al., 2016]. Apart from understanding how power laws may emerge, understanding how they may be deduced from observations, and what may lead to biased estimates, is also important.

We simulate the evolution of the joint floe size and ice thickness distribution, using the FSTD model developed by Horvat and Tziperman [2015, hereinafter HT]. This model explicitly considers how floes are influenced by melting and freezing, ocean surface waves, mechanical interactions between floes (rafting and ridging), and by advection into and out of a given domain. As the HT model is sensitive to a number of different physical processes, we may evaluate whether observed FSD decay characteristics might be explained through the interaction of processes active at different floe length scales. This process-based approach is only one way in which to understand the scaling properties of the FSD. For example, one might suggest a simple deterministic model that predicts a power-law decay as in Toyota et al. [2011]. While this approach can reproduce the phenomenological behavior of some FSD observations, it assumes that the FSD can be represented using a power law. The factors that determine the shape of the FSD are likely more complex and variable. The HT model represents processes acting on individual floes, though it does not account for large-scale ice fracturing, or "linear kinematic features," that can occur within pack ice, and found to be largely scale-invariant [Schulson, 2004].

The HT model has only been evaluated against data qualitatively, due to the aforementioned lack of data on the temporal evolution of the FSD over a wide range of floe sizes. Nevertheless, the HT model is useful in that it allows for (1) examining how the general features of FSD evolution might be determined and evolved using a process-based model, and (2) examining potential biases that arise when assuming power-law FSD behavior, by employing simple observational techniques to the modeled FSD and considering whether these give incorrect estimations of sea ice state variables. A somewhat related model for the FSD was presented by Zhang et al. [2015, hereinafter ZSSS], and was compared to power-law-fits to observations

by Zhang et al. [2016]. This model assumed that all floes of different sizes have the same ITD, and therefore does not represent the dynamics of the coupled thickness and size distribution, and includes only a simplified parameterization of ice breakup from random surface waves. Further context and comparison between the HT and ZSSS models are provided in section 2.

This paper proceeds as follows: we couple a mixed layer ocean model to the FSTD model of Horvat and Tziperman [2015] in section 2. We then consider how the FSD evolves under a variety of external forces and physical processes using a series of experiments in section 3, and discuss the limitations of assuming and analyzing a power law FSD from observations and for future modeling studies and observational analysis. We conclude in section 4.

2. The Discrete FSTD Model

To simulate the evolution of sea ice floes the HT floe size and thickness distribution model [Horvat and Tziperman, 2015] is coupled to a mixed-layer ocean model. The numerical scheme evolves a matrix representation of the floe size distribution, f_{jk} based on a discretization of floe sizes r_j , and thicknesses h_k . The value taken by $f_{jk} \Delta r_j \Delta h_k = f_{jk} (r_{j+1} - r_j) (h_{k+1} - h_k)$ is the area fraction that is covered by floes with size between r_j and r_{j+1} and thickness between h_k and h_{k+1} , and the time evolution of f_{jk} is computed according to,

$$\frac{\mathbf{f}^{i+1} - \mathbf{f}^i}{\Delta t_0} = \mathcal{L}_A(\mathbf{f}^i) + \mathcal{L}_T(\mathbf{f}^i) + \mathcal{L}_M(\mathbf{f}^i) + \mathcal{L}_W(\mathbf{f}^i), \quad (1)$$

where $\Delta t_0 = t_{i+1} - t_i$ is the model time step (see Appendix A, Table 1 for a full list of model parameters). The term \mathcal{L}_A represents the tendency of the FSTD due to ice advection into and out of the domain. The term \mathcal{L}_T is the tendency due to ice thermodynamics and their effects on both the thickness and size of floes. This term accounts for the change to ice concentration due to lateral melting and freezing, which Horvat and Tziperman [2015] pointed out is absent from the ZSSS model. The term \mathcal{L}_M is the tendency due to mechanical interactions between floes. This tendency explicitly accounts for the likelihood of floe collisions that occur when the ice cover is deformed, and also for the formation of new ice floes when two floes either raft or ridge. The representation of ridging in the ZSSS model leads to the formation of thicker floes, as desired, yet not to changes to the FSD. The term \mathcal{L}_W is the tendency due to fracture by ocean surface waves, which carefully accounts for the spectrum and random nature of the ocean wave field and for the attenuation of the surface waves within the ice field. The ZSSS model contains a related fragmentation parameterization that leads to area transfer from large to small floes, however this does not depend on the ocean surface

Table 1. Model Parameters Used in This Study

Variable	Description	Value
Δt_0	Model time-step	1 h
r_{lw}	Width of floe lead region	0.5 m
ρ_a	Atmospheric density	1.275 kg m^{-3}
c_a	Atmospheric specific heat capacity	$1005 \text{ J}(\text{kg}^\circ \text{K})^{-1}$
C_D^i	Turbulent heat transfer coefficient over ice	1.3×10^{-3}
ϵ_i	Sea ice emissivity	1
α_i	Sea ice albedo	0.75
κ_i	Sea ice thermal conductivity	$2.03 \text{ W}(\text{m}^\circ \text{K})^{-1}$
ρ_i	Sea ice density	934 kg m^{-3}
L_f	Sea ice latent heat of melting	334000 J kg^{-1}
α_w	Ocean albedo	0.06
l_0	Fraction of solar radiation absorbed in surface layer	0.45
ϵ_0	Ocean emissivity	0.97
C_D^o	Turbulent heat transfer coefficient over ocean	1×10^{-3}
L_v	Latent heat of vaporization	$2.5 \times 10^6 \text{ J kg}^{-1}$
ρ_w	Ocean density	996 kg m^{-3}
c_w	Ocean specific heat capacity	$4185 \text{ J}(\text{kg}^\circ \text{K})^{-1}$
c_h	Ocean-ice Stanton number	0.06
κ	Ocean vertical eddy diffusivity	$10 \text{ m}^2(\text{d})^{-1}$
κ_w	Extinction coefficient of solar radiation in ocean	0.1 m^{-1}
S_i	Salinity of sea ice	5 psu

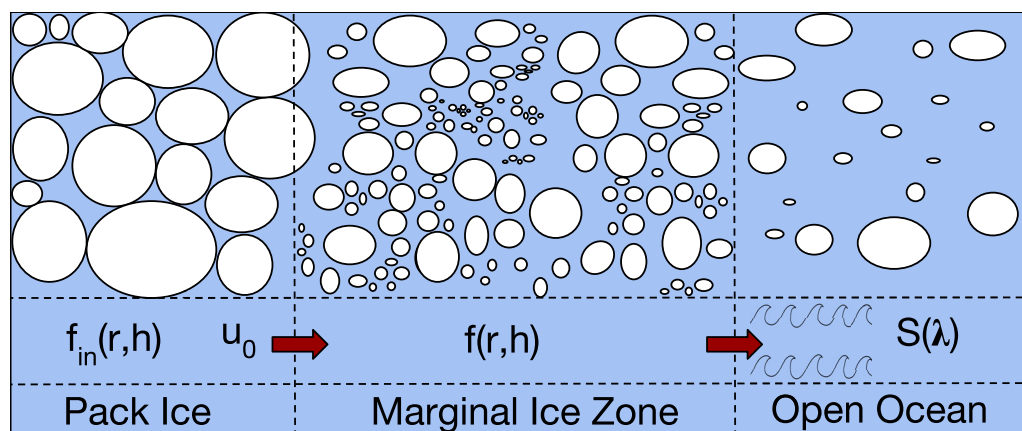


Figure 1. Schematic of the model used in this study. Pack ice with FSTD $f_{in}(r, h)$ is advected into the domain, which represents a marginal ice zone, with a velocity u_0 . Within the model domain the ice is represented through its FSTD $f(r, h)$, and advected into the open ocean with the same velocity u_0 . At the interface with the open ocean, waves with a spectrum $S(\lambda)$ impinge upon the MIZ.

wave spectrum or the interaction of floes with this wave field, as in the HT model. The adaptive scheme used to integrate equation (1) is described in detail in the Appendix A.

2.1. The Coupled FSTD-Ocean Model

We couple the FSTD model to an ocean mixed-layer model following Petty *et al.* [2013]. The specifics of how mixed-layer model variables are computed are given as Appendix B, and a schematic of the mixed layer model is provided in the supporting information Figure S1. The ice has a surface temperature determined diagnostically by the exchange with the atmosphere and ice, and occupies a fraction of the domain equal to the ice concentration, c , computed from the FSTD according to,

$$c = \int_r f(r, h) dr,$$

where the integral is taken over all floe sizes and thicknesses. The ocean model has a surface layer, partitioned into an “open ocean” region and a “lead” region as in Horvat and Tziperman [2015]. The lead region encompasses a thin layer of water surrounding each individual floe, of horizontal width $r_{lw} = 0.5$ m around the floe and of depth 0.1 m below the floe, as in Horvat and Tziperman [2015]. The use of a surface layer that is separate from the mixed layer below provides a more realistic representation of the upper ocean layer thermodynamics as it allows the two to evolve somewhat independently, and thus provides a more realistic framework for the FSTD model, also consistent with the HT model. Others have shown that such a surface layer may be redundant in some climate studies [Petty *et al.*, 2014; Tsamados *et al.*, 2015]. The surface layer thickness is as deep as the lead region and is therefore 0.1 m thicker than the ice. In the lead region, the water temperature is at the freezing point, $T_f \approx -1.8^\circ$ C. For simplicity the freezing temperature does not vary with mixed-layer salinity. The lead region exchanges heat with the open ocean and the mixed layer beneath. In open water areas, the surface ocean layer absorbs a fraction of incoming solar radiation, exchanging heat with the lead region and the mixed layer below, with its temperature determined diagnostically. Below the ice and ocean surface layer lies a mixed-layer that exchanges heat and fresh water with the sea ice, heat with the surface layer, and fresh water with the atmosphere.

The FSTD is discretized into 13 evenly spaced ice thickness categories, with midpoints from 0.2 to 2.7 m, and a maximum floe thickness category with an initial thickness of 2.9 m that is allowed to evolve in order to conserve volume when ice is formed with thickness exceeding that of the thickest category. There are 90 floe size categories, spaced variably according to $r_{n+1} = \sqrt{6/5}r_n$ with midpoints from 0.5 to 1650 m. This variable spacing guarantees that when two floes combine to form a third, the new floe belongs to a floe size category that is distinct from that of the two interacting floes [Horvat and Tziperman, 2015, section 3].

The ocean domain represents a semi-infinite marginal ice zone with a zonal width D , placed between a region of pack ice (say to the west) and a region of open water (to the east) (Figure 1). The pack ice region is characterized by a specified FSTD, f_{in} , and is advected into the MIZ with an ice velocity u_0 . The ice is

advected through the domain, and exits with a specified velocity u . The time rate of change of the FSTD due to advection is therefore,

$$\mathcal{L}_a = \frac{u_0 \mathbf{f}_{in} - u \mathbf{f}}{D}$$

In the experiments that follow, we assume that the two advection velocities are equal. The rate of collisions of floes depends on the shear in the ice velocity, u_y , that we prescribe as an independent parameter that does not affect the zonal advection. To the east, the MIZ borders open water, where a surface wave field represented by a spectrum $S(\lambda)$ reaches the MIZ.

2.2. Evaluating Whether the FSD Decays as a Power Law

We wish to understand the evolution of scaling behavior in the FSD. *Perovich and Jones* [2014] examined how the slope of a power-law FSD might be determined from visual imagery. Ignoring ice thickness, consider a floe size distribution, $f(r)$, where $f(r) dr$ is the fraction of the ocean surface covered by floes with a size between r and $r + dr$. Suppose this FSD decays as a power-law, $f_0 r^{-\alpha}$ within the range of floe sizes from r_1 to r_2 , where f_0 is a suitable normalization coefficient such that $\int_0^\infty f(r) dr = c$ is the ice concentration. Assume without loss of generality that there are no floes with size outside the range from r_1 to r_2 . The ice concentration, c , and floe perimeter per square meter, P , are calculated,

$$c = \int_{r_1}^{r_2} f_0 r^{-\alpha} dr = \frac{f_0}{1-\alpha} (r_1^{1-\alpha} - r_2^{1-\alpha}) \approx \frac{f_0}{1-\alpha} r_1^{1-\alpha}, \tag{2}$$

$$P = \int_{r_1}^{r_2} \frac{2\pi r f_0 r^{-\alpha}}{\pi r^2} dr = 2 \frac{f_0}{\alpha} (r_1^{-\alpha} - r_2^{-\alpha}) \approx \frac{2f_0}{\alpha} r_1^{-\alpha}, \tag{3}$$

where we assume $r_2 \gg r_1$. This formulation may also be applied over any range of floe size from r_1 to r_2 by regarding c and P as the ice concentration and floe perimeter per square meter belonging to floes with size between r_1 and r_2 . With c and P known, the power-law exponent was computed by *Perovich and Jones* [2014] as,

$$\alpha = \left(1 - \frac{r_1 P}{2c} \right)^{-1}. \tag{4}$$

Both c and P may be computed readily from visual imagery of the ice surface. Therefore, if the FSD decays like a power law, equation (4) can be used to determine the power-law slope from observations without using more complex image-processing algorithms to identify individual floes.

The assumption of a power-law FSD implied in equation (4) is not necessarily valid. However, with access to the full time-evolving FSD we can examine drawbacks of this assumption, comparing the results of applying equation (4) to other techniques for estimating the FSD slope.

The first alternative method is a simple least-squares fit to the modeled FSD. This method often produces inaccurate estimations of the power law decay coefficient *Clauset et al.* [2009] and no information regarding whether the underlying distribution decays as a power law at all. Further, this form of regression is often erroneously applied to the cumulative distribution function, which is concave-down, and is therefore not a straight line in log-log space. In the sections that follow the least-squares fitting is applied in all cases to the FSD itself.

The previous methods require that the minimum floe size over which the FSD decays as a power law be specified. The second alternative method employs the maximum likelihood estimator (MLE) as outlined by *Clauset et al.* [2009] and demonstrated in *Virkar and Clauset* [2014]. This method is the most accurate method for identifying the minimum floe size at which the tail begins, and the slope of the power-law tail. Since the MLE is computed from observational data, when it is applied, we generate 50,000 synthetic floe size observations from the model output, estimating the most likely power-law slope.

These three methods estimate the decay exponent of a power-law decaying FSD, and the simplest statistical test for power-law decay is that all estimate approximately the same value for α . These types of comparisons can test for biased estimates of power-law slope. Each estimate, however, assumes that the underlying

distribution is a power law, a hypothesis that must be tested statistically. Virkar and Clauset [2014] outline an approach for this test using binned observations, and in section 3.2 we examine a simple hypothesis test using model data, comparing different distributional fits to the FSD.

In the results that follow, we evaluate how FSTD model output compares to the estimate (4), to understand how and when a power-law FSDs may emerge. We use this comparison to examine the scenarios under which equation (4) can be used to analyze power-law FSD in observations.

3. Results

We proceed as follows: we consider how mean quantities that are derived from the FSTD may evolve in different and nonintuitive ways in section 3.1. We then consider how the individual forcing fields of thermodynamics, mechanics, and wave fracture affect a floe size distribution that is initially a power law in sections 3.2–3.4. Finally, running the model using all forcing fields combined, we consider how different regimes emerge at different floe length scales in section 3.5.

3.1. Influence of Sea Ice Advection on Mean Quantities Derived From the FSTD

Consider first the evolution of an FSTD forced only by the advection of ice from the pack ice region and then out of the domain, with a constant velocity $u = 10$ cm/s. In this case we do not yet use the mixed layer model developed in Appendix B. The evolution of the FSTD may be solved for analytically in this case. Despite this simple context, the evolution of some important quantities derived from the FSTD is nonintuitive, emphasizing the importance of comprehensively understanding the FSTD before parameterizing its evolution in climate studies.

Let the initial FSTD, $f(\mathbf{r}, t=0)$, be a narrow Gaussian centered at a floe size of 5 m and a thickness of 1 m, with an ice concentration of 25%. The incoming pack ice FSTD, $f_{in}(\mathbf{r})$, is a narrow Gaussian centered at a floe size of 150 m and floe thickness of 2 m. The standard deviation of each Gaussian is 5 m in floe size and 0.1 m in ice thickness. We choose these initial distributions for simplicity, however the results that follow are general and apply to any case where advection acts on the FSTD. The domain width D is 10 km.

The FSTD, $f(\mathbf{r}, t)$, evolves according to,

$$\frac{\partial f(\mathbf{r}, t)}{\partial t} = \frac{u}{D} (f_{in}(\mathbf{r}) - f(\mathbf{r}, t)),$$

with a solution,

$$f(\mathbf{r}, t) = f_{in}(\mathbf{r}) + (f(\mathbf{r}, t=0) - f_{in}(\mathbf{r})) \exp(-ut/D).$$

The FSTD approaches the pack ice FSTD, $f_{in}(\mathbf{r})$, exponentially at all sizes and thicknesses, with a timescale $\tau_{adv} = D/u = 1.15$ days. Figures 2a–2d show how four sea ice model variables evolve over the first 12 days: ice concentration, c (Figure 2a), ice volume per square meter, V (Figure 2b), mean ice thickness per unit area, $\bar{h} = V/c$ (Figure 2c), and mean floe size, \bar{r} (Figure 2d). The mean floe size is computed using the number distribution of floes, $N(\mathbf{r})$,

$$N(\mathbf{r}) = \frac{f(\mathbf{r})}{\pi r^2},$$

where $N(\mathbf{r})d\mathbf{r}$ is the number of floes per square meter with floe size between \mathbf{r} and $\mathbf{r} + d\mathbf{r}$,

$$\bar{r} = \frac{\int_{\mathbf{r}} N(\mathbf{r}', t) r' d\mathbf{r}'}{\int_{\mathbf{r}} N(\mathbf{r}', t) d\mathbf{r}'} \tag{5}$$

and the subscripts indicate an integral over all floe sizes and thicknesses. This definition is simply related to the total floe perimeter within a grid cell, which is necessary to determine the strength of lateral melting, as $2\pi\bar{r}\mathcal{N}$, where $\mathcal{N}(t)$ is the number of floes per unit area. The mean floe size may also be defined as an area-weighted average, replacing $N(\mathbf{r})$ with $f(\mathbf{r})$ in equation (5), but this mean size is not related to key metrics such as the total perimeter. In any case, the mean floe sizes based on both $f(\mathbf{r})$ and $N(\mathbf{r})$ are shown in Figure 2d.

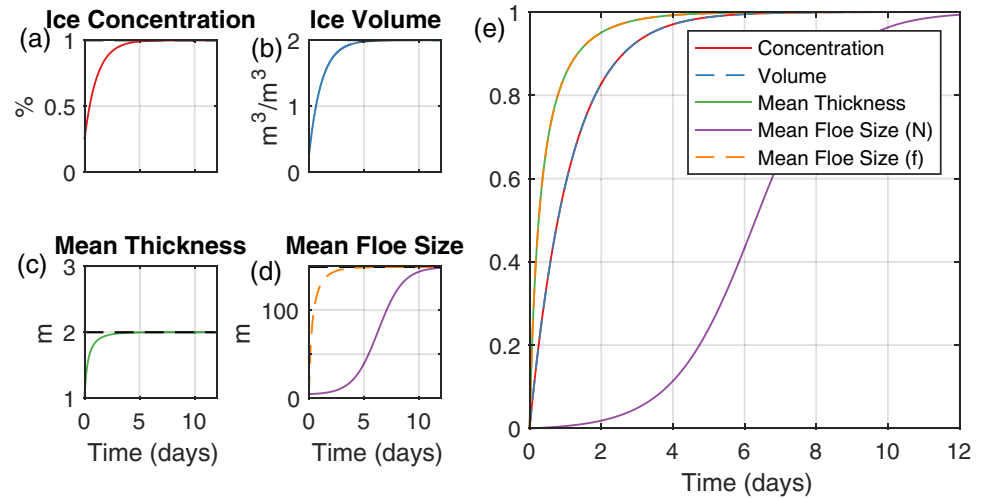


Figure 2. The evolution of four sea ice variables subject to advection through the model domain. (a) Ice concentration. (b) Ice volume per square meter. (c) Mean ice thickness. (d) Mean floe size, computed either from the floe size distribution (dashed line) or the floe number distribution (solid line). Dashed black lines correspond to pack ice values advected into the domain. (e) Time series of the normalized distance between each variable in (a-d) and its corresponding pack ice value, computed as $(x - x_{in}) / (x_0 - x_{in})$, where x_0 is the initial value of variable x , and x_{in} the corresponding pack ice value. Shown are averages based on both the number distribution (N) and FSD (f).

Despite the exponential approach of the FSTD at all sizes to the pack ice FSTD, the above four mean model variables do not approach their corresponding pack ice values at the same rate. To quantify the difference in the evolution of the different variables, we compute and plot (Figure 2e) the approach of each variable, normalized as $(x - x_{in}) / (x_0 - x_{in})$, where x_0 is the initial value of variable x , and x_{in} the corresponding pack ice value. Sea ice concentration (red) and volume per square meter (blue) approach the pack ice sea-ice values over a timescale τ_{adv} . Neither the mean ice thickness per unit area nor mean floe size (Figures 2c and 2d), approach their steady state at this rate. Mean ice thickness approaches the mean ice thickness of the pack ice *faster* than does ice volume per unit area or concentration (Figures 2c and 2e, green line). Mean floe size does not follow an exponential approach, approaching the pack ice mean floe size much slower than the other variables considered here (Figures 2d and 2e, purple line).

The time evolution of the mean size \bar{r} is obtained from equation (5),

$$\frac{\partial \bar{r}}{\partial t} = \frac{\int_{\mathbf{r}} \frac{\partial N}{\partial t} \mathbf{r}' d\mathbf{r}' \int_{\mathbf{r}} N d\mathbf{r}' - \int_{\mathbf{r}} N \mathbf{r}' d\mathbf{r}' \int_{\mathbf{r}} \frac{\partial N}{\partial t} d\mathbf{r}'}{\left(\int_{\mathbf{r}} N(\mathbf{r}', t) d\mathbf{r}' \right)^2} \quad (6)$$

$$= \frac{\mathcal{N}_{in} \bar{r}_{in} - \bar{r}}{\tau_{adv} \mathcal{N}(t)}$$

where \bar{r}_{in} is the mean floe size of the pack ice FSTD, $\mathcal{N}(t)$ is the number of floes per unit area, and \mathcal{N}_{in} is the number of floes per unit area in the incoming pack ice, and integrals are taken over all floe sizes and thicknesses. The initial growth of the mean floe size is determined by the time-scale $\tau_{adv} \mathcal{N}_0 / \mathcal{N}_{in} \approx 200$ days, which varies, approaching τ_{adv} as $\mathcal{N}(t)$ approaches \mathcal{N}_{in} . When there are fewer floes per unit area in the pack ice than in the MIZ represented by the model domain (as is the case in this experiment), this time-scale is larger than τ_{adv} . The mean ice thickness evolution is found as,

$$\frac{\partial \bar{h}}{\partial t} = \frac{c_{in} \bar{h}_{in} - \bar{h}}{\tau_{adv} c(t)},$$

and its initial growth is determined by the timescale $\tau_{adv} c_0 / c_{in} \approx 7$ h, which also varies, approaching τ_{adv} as c approaches c_{in} .

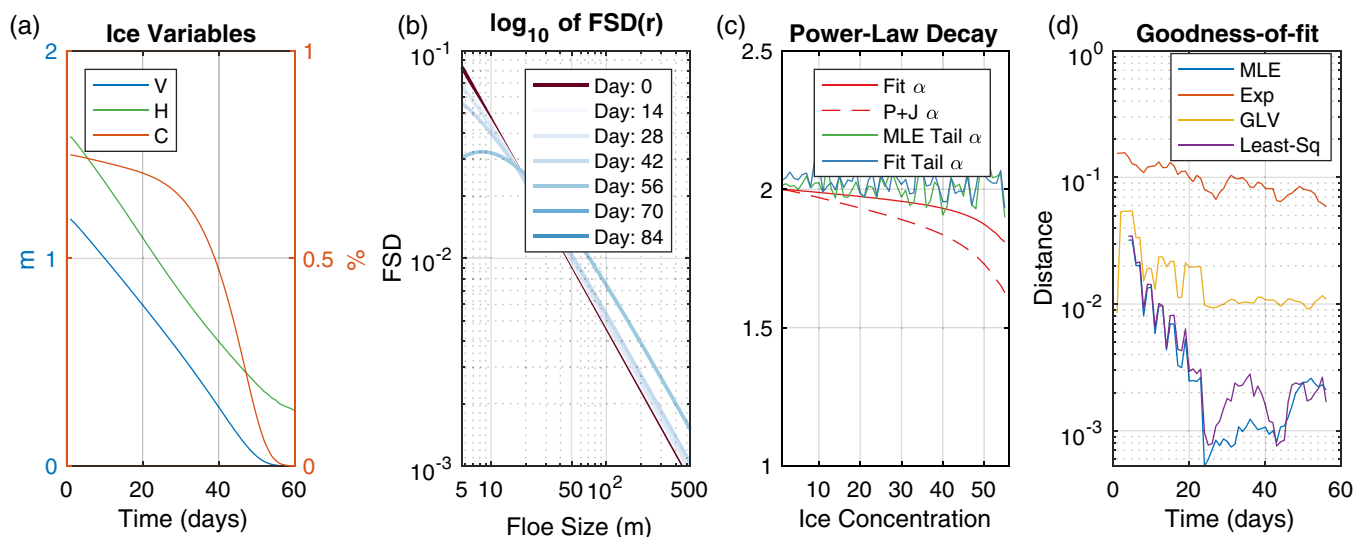


Figure 3. Evolution of the FSTD subjected to ice melting only. (a) Time evolution of sea ice concentration (in percent), ice volume per unit area and mean ice thickness (in m). (b) Log-log plot of the evolution of the FSD, normalized to one, over time. Red line is initial FSD. (c) Power-law exponent fits: least squares fit over the range from 5 to 500 m (solid red line), predicted value from equation (4) (dashed red line), maximum likelihood estimate for the distributional tail, with the tail identified using the method of *Virkar and Clauset* [2014] (green line), and least-squares fit to the tail of the distribution (blue line). (d) Comparison of Kullback-Leibler divergence (equation (8)) between the modeled FSD and the maximum likelihood estimate of *Virkar and Clauset* [2014] (blue line), an exponential fit (red line), a generalized Lotka-Volterra fit (purple line) [*Herman*, 2011], and a least-squares fit to the FSD tail.

This simple example demonstrates how mean important diagnostics for the sea ice cover, which are computed as moments of the ITD (in the case of mean thickness), FSD (in the case of mean floe size), or FSTD (both) may evolve quite differently in time from one another even when one expects simple behavior. Sea ice models compute the evolution of ice volume, V , and ice concentration, c , and so the mean ice thickness, $\bar{h} = V/c$, can be diagnosed without evolving the FSD. However mean floe size cannot be similarly related to sea ice state variables. Climate models that do not parameterize the full evolution of the floe size distribution, but still require information about the sub-gridscale variability of floe size for use in parameterizations (e.g., of the floe-size dependent melting rate [*Steele*, 1992; *Horvat et al.*, 2016]), must take this into account before evolving mean floe size as a potential state variable.

3.2. The Influence of Lateral Melting on the Floe Size Distribution

We now consider how the FSTD evolves subject to thermodynamic forcing alone, such that floe sizes are only affected by lateral melting, as in the study of *Perovich and Jones* [2014]. The HT model geometrically partitions net surface heat fluxes into those that are close to sea ice floes and those that lead to ocean surface warming and cooling. Those fluxes that influence floe development are further partitioned into components that lead to lateral and basal growth or melting. Details on the partitioning scheme are found in *Horvat and Tziperman* [2015, section 2.1], and details of the ice thermodynamic model are given in Appendix section B3.

To force the model, we use atmospheric fields from the NCEP-II [*Kanamitsu et al.*, 2002] climatology at the location of the SHEBA ice camp at 78N, 166 W, in July. The atmospheric temperature is 0.5°C , the atmospheric specific humidity is 3.6 g/kg, the surface pressure is 1010 hPa, and the atmospheric wind speed is 1 m/s. There is precipitation in the form of rain of $1\text{ mm/m}^2/\text{d}$ reaching the ocean. There is 290 W/m^2 of shortwave radiative forcing, and 270 W/m^2 of downward long-wave radiative forcing. The deep ocean temperature is prescribed at -1.8°C , the deep ocean salinity is prescribed at 33 PSU, and the mixed layer temperature and salinity are initialized at these values. The ocean mixed layer depth is 30 m. The initial floe size distribution is the product of a power-law in floe size from 5 to 1500 m, with an exponent of -2 and a Gaussian ice thickness distribution centered at 1 m thickness, with an initial ice concentration of 75%.

Figure 3a shows the evolution of ice concentration (red line, right axis), ice volume per square meter (blue line, left axis) and mean ice thickness (green line, left axis) over the course of this simulation. The surface ocean is warmed by the external forcing fields by 116 W/m^2 per unit area of open water (equation (B4)). As the initial ice-free fraction is 25%, this corresponds to an initial average over the entire domain area of 29

W/m². The sea ice melts over a 50 day period, and as the concentration decreases, more heat is absorbed into the surface layer. The sea ice melts due to warming at the ice surface with an average (averaged over both time and the FSTD) magnitude of 13 W/m² (calculated from equation (B1)), warming at the ice base with an average magnitude of 2 W/m² (calculated from equation (B5)), and a dominant warming from the lead region with an average magnitude of 61 W/m² (calculated from equation (B6)).

Blue lines in Figure 3b show the FSD as function of floe size every two weeks, normalized such that it integrates to one to allow for a comparison of the FSD shape between different times, as the ice area decreases. Over time, the slope of the FSD shallows and deviates from a power law at small floe sizes, similar to the deviation from power law at small floe sizes found in observations by *Perovich and Jones* [2014]. The evolution of a floe size distribution $f(r)$ subjected to only melting (equation (4)) [*Horvat and Tziperman*, 2015] is,

$$\frac{\partial f(r, t)}{\partial t} \Big|_{\tau = G_r} \left(-\frac{\partial f(r)}{\partial r} + \frac{2}{r} f(r) \right), \tag{7}$$

where $G_r < 0$ is the lateral melting rate. The first term in (7) represents the movement of floes between size classes as they change their size, and the second term represents how, as floes change their size, they also change their area and therefore the shape of the FSD. For an initial power-law FSD $f(r, 0) = f_0 r^{-\alpha}$, the solution, $f(r, t)$ is obtained using the method of characteristics,

$$f(r, t) = f_0 \frac{r^2}{(r + |G_r|t)^{2+\alpha}} \approx f_0 r^{-\alpha} \left(1 - (\alpha + 2) \frac{|G_r|t}{r} \right).$$

The second term in parentheses, being a function of the floe size r and proportional to time, is responsible for deviation from power law at sufficiently long times. We define the timescale, $\tau_{PL} = \bar{r} / ((\alpha + 2)|G_r|)$, over which the FSD departs from its power-law behavior for scales up to the mean floe size. During this simulation, lateral melting rates are $G_r \sim 5$ cm/d, and the initial mean floe size is $\bar{r} \sim 30$ m. With $\alpha = 2$, we therefore have $\tau_{PL} \approx 150$ days. The timescale over which ice volume melts is set by the vertical melt rate, which in these simulations is $G_h \approx 2$ cm/d. With an initial mean thickness $\bar{h} = 1$ m, the ice therefore melts over a period of 50 days $< \tau_{PL}$. Lateral melting therefore does not cause the FSD to deviate from its initial power-law behavior before it melts completely, for scales up to the mean floe size.

If the FSD were to deviate significantly from a power law, we expect a difference between the least-squares fit to the model output in Figure 3b and the power-law prediction from equation (4). Figure 3c shows this comparison, plotting the value of α computed by fitting the FSD to a straight line in log-log space from 5 to 500 m (solid), compared to α evaluated using equation (4), where $r_1 = 5$ m (dash). In general, lateral melting reduces the fit slope of the FSD over this range from 2 to 1.75 over the course of the simulation. Smaller floes melt most significantly, and lead to a deviation in the power-law slope that is shown as an increasing difference between the computed power-law exponent and α in Figure 3c. The maximum relative error between α_{est} and α is small, just 7%, as the influence of this lateral melting is not significant at the scale of the mean floes, as predicted above when comparing the timescale of ice melt to the timescale, τ_{PL} , over which the FSD deviates from a power law.

We also compute an estimate of the power-law tail using the method of *Virkar and Clauset* [2014] (Figure 3b, green line). To do so, we generate a set of synthetic floe sizes following the distribution $f(r)$, computing the maximum likelihood estimates of the power-law exponent α and minimum floe size r_{min} over which the tail of the distribution from $r_{min} \rightarrow \infty$ decays as a power law. We fit this synthetic data to three alternative distributions: a naive least-squares fit to the binned synthetic data (Figure 3b, green line), an exponential distribution, and the “generalized Lotka-Volterra” distribution hypothesized by *Herman* [2011].

For each fit $\tilde{g}(r)$ we compute the KullBack-Leibler divergence,

$$D_{KL}(f || \tilde{g}) = \int_{r_{min}}^{\infty} f(r) \log \frac{f(r)}{\tilde{g}(r)} dr, \tag{8}$$

a measure of the information lost when substituting the hypothesized distribution \tilde{g} for the actual model distribution f [*Joyce*, 2011]. When $D_{KL} = 0$, the hypothesized distribution accurately captures the real distribution, while when $D_{KL} = 1$ the misfit is maximal in this measure. We test whether the hypothesis of a

power-law tail is appropriate by comparing the values of D_{KL} for different fits to the distribution f . Since the lateral melting is most effective at smaller scales, the tail of the distribution retains a power-law slope of -2 (Figure 3b). Computing D_{KL} reveals that the distributional tail is better fit by a power law than a GLV or exponential distribution, as expected (Figure 3d). Revealingly, the maximum likelihood estimator is a better fit to the modeled distribution than a simple least-squares fit to the binned data, as demonstrated by *Virkar and Clauset* [2014].

The above discussion suggests that lateral melting may alter the shape of the FSD if the ratio of τ_{PL} to the melting time scale, $\bar{r}G_h/(\bar{h}|G_r|(2+\alpha))$ is small. This ratio is related to the (large) aspect ratio of average floes, \bar{r}/\bar{h} . Typically, parameterizations of lateral melting used in sea ice models [*Steele, 1992; Horvat and Tziperman, 2015*], determine the partitioning of a net heat flux between lateral and vertical melting using this aspect ratio. This is because the total surface area between a floe and the ocean surrounding it consists of a lateral part of area $2\pi rh$ and a basal part of area πr^2 , with a ratio $2h/r$. If the heat flux between the ocean and the ice is diffusive, this ratio determines how much heat from the ocean will go into the lateral versus the basal edge of floes. When this aspect ratio is large, a power-law FSD impacted by lateral melting alone will maintain its shape, and the computation of α via equation (4) will be accurate. However, *Horvat et al.* [2016] found that this commonly used diffusive partitioning may significantly underestimate the lateral melting for large floes because it does not include the effect of ocean eddies. In such situations, where ocean eddies significantly contribute to the effective lateral melting, the FSD is expected to quickly deviate from a power law.

3.3. The Influence of Floe Collisions on the Floe Size Distribution

We next examine how mechanical interactions between floes influence the FSTD evolution. The HT model considers the statistical likelihood that two floes collide as the ice cover undergoes deformation, allowing for floes to raft or ridge with one another and former larger, conglomerate floes. Details can be found in *Horvat and Tziperman* [2015, section 2.2].

To force the model, we prescribe a mean ice velocity, $u_0 = 10$ cm/s, that advects the FSTD through the model domain as described in section 3.1. The ice velocity field has a prescribed shear component with magnitude $|u_y| \sim u_0/D = 2 \times 10^{-6}$ 1/s. The thermodynamic component of the FSTD model considered in section 3.2 is not active. The initial FSTD, $f_0(\mathbf{r})$, and the incoming pack ice FSTD, $f_{in}(\mathbf{r})$, are the product of a power-law FSD between floe sizes 5–1500 m with slope $\alpha = 2$, and an ice thickness distribution that is a Gaussian centered at 1 m. The pack ice FSTD has 100% ice concentration, whereas the initial FSTD has 75% ice concentration.

The shearing ice velocity field leads to differential ice motions, collisions, and interactions between floes. Figure 4a shows the evolution of the ice state variables of concentration, volume per unit area, and ice thickness. Mechanical interactions between floes lead to uplift (ridging and rafting) of ice and therefore reduce the ice concentration. The time rate of change of concentration $\left. \frac{\partial c}{\partial t} \right|_{coll}$ due to this deformation is [*Thorndike et al., 1975; Horvat and Tziperman, 2015, section 2.2, equation (B5)*],

$$\left. \frac{\partial c}{\partial t} \right|_{coll} = -\frac{u_0}{2D} = -5 \times 10^{-7} \text{ 1/s.}$$

The time rate of change of ice concentration is therefore determined by the balance between the advection of new ice concentration and the reduction of ice concentration due to collisions, and can be solved for analytically as follows,

$$\frac{\partial c}{\partial t} = -\frac{u_0}{2D} + \frac{u_0}{D}(c_{in} - c) = \frac{u_0}{D} \left(\frac{1}{2} - c \right),$$

where $c_{in} = 1$ is the incoming pack ice concentration. The steady-state solution is $c = 1/2$, thus due to these mechanical interactions the FSTD reaches a steady-state ice concentration of 50%.

Collisions between floes shape the FSD by transferring ice area from smaller floe sizes to larger ones. Both the initial and advected FSDs, $f_0(\mathbf{r})$ and $f_{in}(\mathbf{r})$, have power-law slopes of -2 . However, when examining the transient evolution of the FSD, we note that it deviates from a power-law behavior (Figure 4b, blue lines). At later times, the distribution becomes more power-law-like, and results in a shallower sloping distribution (Figure 4b, darkest blue line). Using a least-squares fit, the steady-state distribution is fit to a power-law

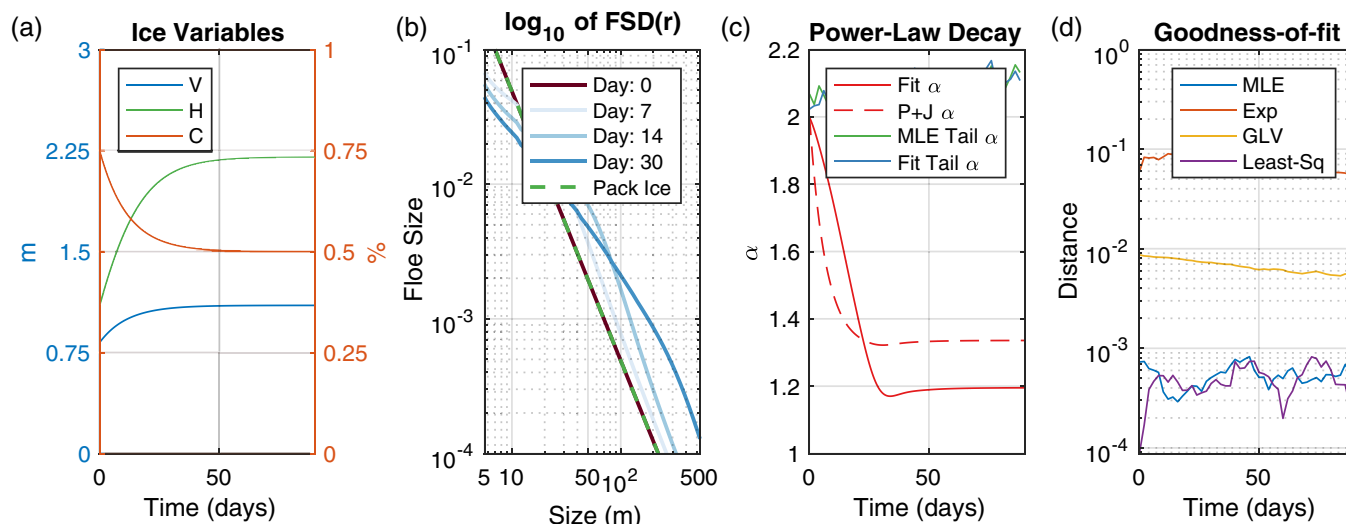


Figure 4. Evolution of the FSTD during mechanical floe interactions. (a) Time evolution of sea ice concentration (in percent), ice volume per unit area and mean ice thickness (in m). (b) Log-log plot of the evolution of the FSD, normalized to one, over time. Red line is initial FSD. Green line is pack ice FSD. Darkest blue line is final FSD. (c) Power-law exponent fits: least squares fit over the range from 5 to 500 m (solid red line), predicted value from equation (4) (dashed red line), maximum likelihood estimate for the distributional tail, with the tail identified using the method of *Virkar and Clauset* [2014] (green line), and least-squares fit to the tail of the distribution (blue line). (d) Comparison of Kullback-Leibler divergence (equation (8)) between the modeled FSD and the maximum likelihood estimate of *Virkar and Clauset* [2014] (blue line), an exponential fit (red line), a generalized Lotka-Volterra fit (purple line) [*Herman*, 2011], and a least-squares fit to the FSD tail.

slope of $\alpha=1.2$ (Figure 4c, solid line) over the floe size range from 5 to 500 m. The FSD tail, however, steepens over time (Figure 4b, green and blue lines), and the least-squares fit exponent has a lower KL divergence from the modeled FSD compared to the MLE when considering the tail of the distribution (Figure 4d), though both are significant improvements over a possible exponential fit or generalized Lotka-Volterra fit. The transient behavior implies that variability in the strengths of mechanical interactions between floes (e.g., due to changes in shear or convergence) will lead to deviations from a power law FSD over large size ranges, but a power-law tail is maintained.

Comparing α calculated via equation (4) to the power-law fit over 5–500 m α_{est} shows, indeed, that the difference between the two starts at zero when the behavior exactly follows a power law. The error increases as the FSD deviates from a power law over the first 10 days, approaching a steady-state after 20 days (Figure 4c, solid line). There is weaker agreement between the two than in the case of pure thermodynamic forcing. The relative error between α and α_{est} now exceeds 15% during the first 20 days, during which time the FSD is not well-approximated by a power law at steady state, equation (4) predicts a slope of 1.34, for a relative error of 11%. For comparison, the implied difference in total floe perimeter for power-law FSDs with slopes $\alpha=1.34$ or $\alpha=1.2$ between $r=5$ to $r=500$, and 100% ice concentration, is between roughly 160 and 190 km of floe perimeter per square kilometer of ocean surface, which may affect estimated lateral melt rates.

3.4. The Influence of Wave Fracture on FSD Slope

We next explore how ice fracture by ocean surface waves affects the FSTD. The HT model explicitly simulates the evolution and attenuation of sea surface height within the ice cover based on the wave spectrum reaching on the ice, computing locations of maximum strain. Floes are assumed to flex with the sea surface height, and when the strain felt by floes exceeds a critical threshold, they break, as in *Dumont et al.* [2011]. Full details of the parameterization are provided in *Horvat and Tziperman* [2015, section 2.3].

We consider again ice advected into and out of the domain with a velocity $u = 10$ cm/s, but no shear or divergence and therefore no mechanical interactions between floes, and no melting. At the ice edge, a monochromatic swell wave spectrum, with a peak wavelength $\lambda = 100$ m is applied to the ice field. This ocean wave spectrum fractures large floes into floes with a preferred size of $\lambda/2 \approx 50$ m.

The fracture of floes by ocean surface waves reduces the mean floe size (Figure 5a) and steepens the floe size distribution by breaking floes of size larger than $\lambda/2$ (Figure 5b, blue lines). Floes larger than 50 m are

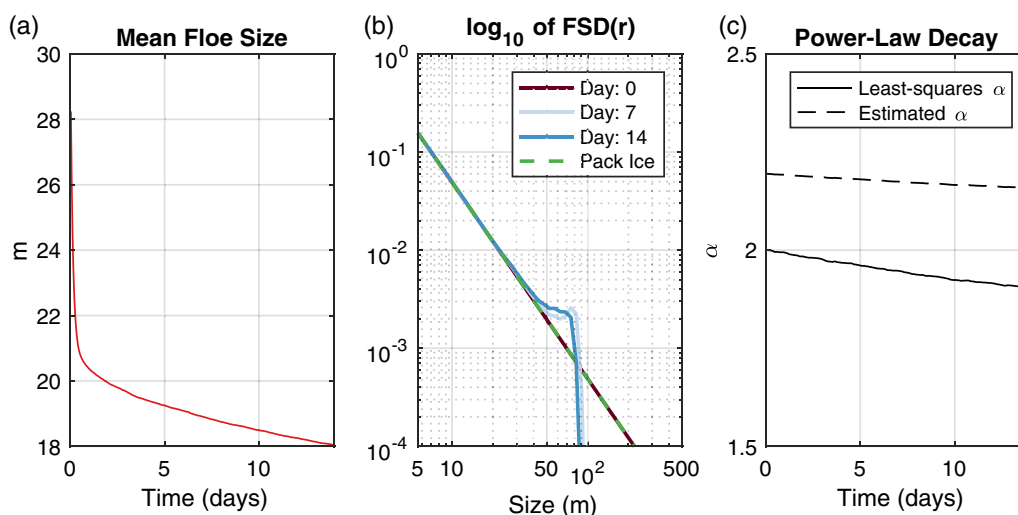


Figure 5. Evolution of an FSTD fractured by surface waves. (a) Mean floe size over time (m). (b) Log-log plot of the evolution of the FSD, normalized to one, over time. Red line is initial FSD. Green line is pack ice FSD. Darkest blue line is final FSD. (c) Comparison of power-law fit to simulated FSD with analytical estimates. Black solid line is the numerical fit to the simulated FSD over the range from 5 to 50 m. Dashed solid line is the result obtained via equation (4) over the range 5–50 m.

fractured by the waves, so therefore we expect there to be two regimes, one composed of floes smaller than 50 m, and one composed of floes larger than 50 m. We therefore compute a least-squares power-law fit to the FSD over the floe size range from 5 to 50 m, finding a gradual decrease in the slope computed from a least-squares fit, from $\alpha = 2$ to $\alpha = 1.8$, as new floes are formed with a size near 50 m (Figure 5c, solid line). Since the FSD clearly does not exhibit a power law tail we do not apply the method of *Virkar and Clauset* [2014].

The value of α evaluated using equation (4) over the range between 5 and 50 m (dashed line, Figure 5c) is inaccurate, estimating a power law slope roughly 0.25 greater, even at $t = 0$, when the FSD is prescribed to be a power law. This discrepancy results from the approximation that the size range of the power law decay is wide, $r_2 \gg r_1$, used in equations (2) and (3) to derive the expression for α in equation (4). When the computation of α is extended over the range from 5–500 m, the method is accurate at $t = 0$. Yet at later times, extending the range to 500 m cannot give an accurate approximation because the behavior is not of a power law beyond sizes of about 50 m.

These results demonstrate an important limitation of the approximations used by *Perovich and Jones* [2014] to derive the simple expression (4) for the power-law decay of the FSD. Equation (4) is inaccurate when considering a single decade of floe size, as the small tail of the FSD can bias the estimated power law, even when the behavior is exactly a power law, as it is at $t = 0$ in the above simulation. Many observations of the FSD only resolve a small range of floe sizes, and therefore estimates based on (4) may be biased when a small window of floe sizes is resolved. In that case, one may need to solve equations (2) and (3) numerically, though it may be safer to estimate the actual distribution shape, rather than assuming a power law decay, given that the FSD evolution demonstrated in Figure 5b is not power-law-like over the range of floe sizes considered here.

3.5. Determination of the FSD Structure When Sea Ice Is Subject to Several Forcing Fields

Having explored each physical process individually, we next simulate the evolution of the FSTD when all external forcing fields are active, and examine the steady-state balances between the different physical processes, at different floe length scales. Both the incoming FSTD and initial FSTD are the product of a Gaussian ice thickness distribution centered at 1 m thickness and a power-law FSD with exponent -2 over the range from 5 to 1500 m. In supporting information Text S1 and Figure S2, we examine the sensitivity of the results presented below to \mathbf{f}_{in} . In general, the qualitative behavior of the FSTD that develops is insensitive to the slope of the pack ice FSD. The incoming pack ice concentration is 100%, and the initial FSTD concentration is 75%. The thermodynamic forcing is the same as in section 3.2, and the mechanical forcing and advective

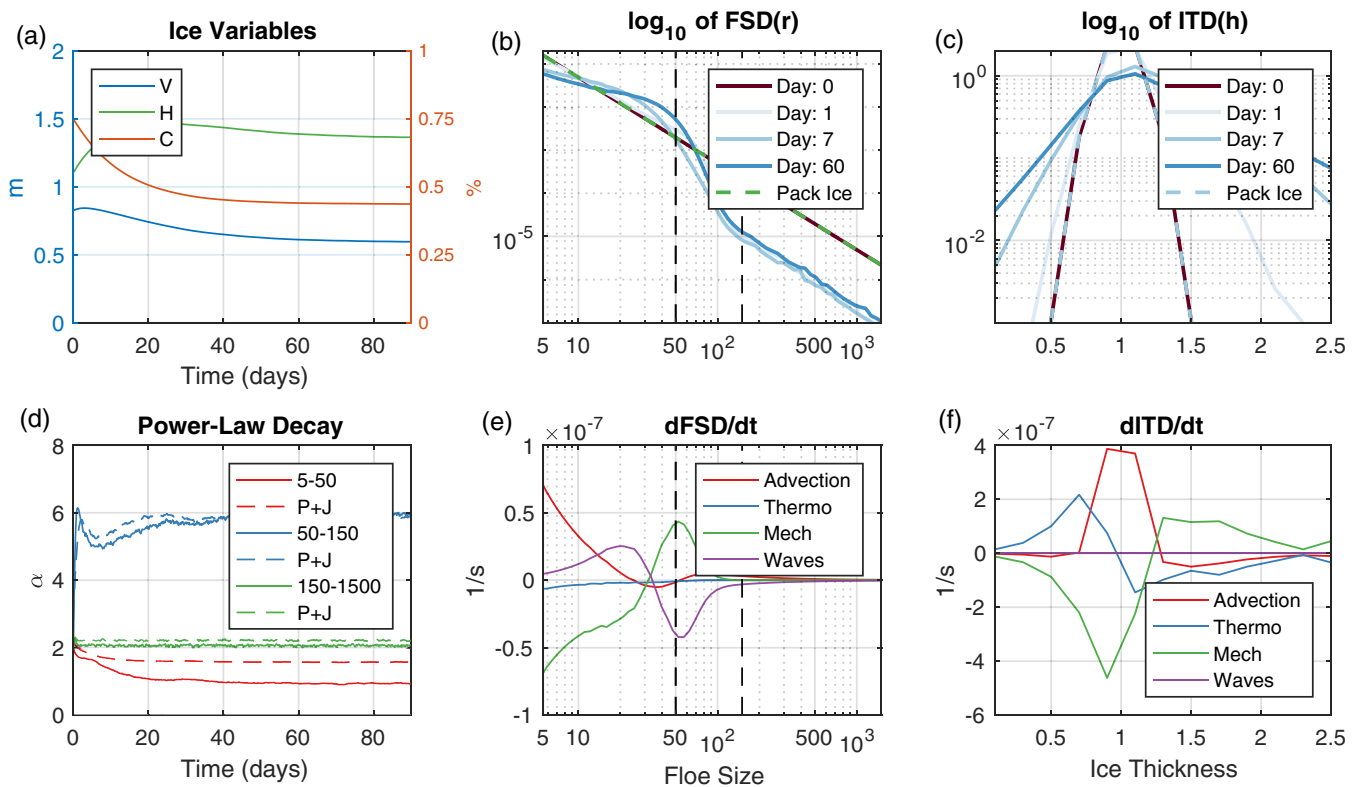


Figure 6. Evolution of the FSTD forced by melting, ice advection, mechanical interactions between floes, and fracture by ocean surface waves. (a) Time evolution of sea ice concentration (right axis), ice volume per unit area and mean ice thickness (m, left axis). (b) Log-log plot of the evolution of the normalized FSD, over time. Red line denotes the initial FSD. Green line denotes the incoming pack ice FSD. Darkest blue line represents the steady state FSD. Vertical dashed black lines separate the three distinct regions of power law scaling. (c) Log-log plot of the evolution of the normalized ITD over time. Red line shows the initial ITD, green line the pack ice ITD, darkest blue line the steady state ITD. (d) (solid lines) Power-law exponent fit to the FSD over the three scaling regimes identified in Figure 6b, from 5 to 50 m (red), 50 to 150 m (blue) and 150 to 1500 m (green), compared to the prediction of equation (4) (dashed lines). (e) The FSD tendency due to each physical process in the FSTD equation (1), averaged over the final week of the simulation. (f) Same as Figure 6d, but for the ITD.

velocities are the same as in section 3.3. We choose as an ocean surface wave field a realistic Bretschneider wave spectrum [Michel, 1999],

$$S(\lambda) d\lambda = \frac{H_s^2}{8} \frac{\lambda}{\lambda_z^2} e^{-\frac{1}{2}(\frac{\lambda}{\lambda_z})^4} d\lambda,$$

where $H_s = 2$ m is the significant wave height, and $\lambda_z = 50$ m is the average distance between zero-crossings of the wave record.

Figure 6a shows the evolution of ice concentration, ice volume per unit area, and mean ice thickness. In response to the presence of both collisions and melting, the ice concentration reaches a steady-state value of 42%, lower than in the simulation in which only collisions are active (Figure 4a, red line). Initially, mechanical interactions between floes increase the ice thickness and open water fraction. The increased open water fraction leads to greater heating of the sea ice as more heat is absorbed by the ocean surface layer, and this reduces the mean ice thickness to a steady-state value of 1.36 m (Figure 6a, green line). Ice volume per unit area is not influenced by ice fracturing or mechanical collisions, and achieves a steady-state balance between melting and volume advection of $0.6 \text{ m}^3/\text{m}^2$.

Figure 6b plots the floe size distribution (normalized to integrate to 1) at days 1, 7, and 60, as well as the initial and incoming pack ice FSD (red and dashed green lines). Over time, three distinct regimes emerge, labeled I-III in Figures 6b and 6e. The three regimes are: (I) a shallow, decaying regime from $r_1-r_2=5-50$ m, (II) a steeper decaying regime from $r_1-r_2=50-150$ m, and (III) an intermediate decaying regime from $r_1-r_2=150-1500$ m. The modeled floe size distributions shown in Figure 6b are scale-dependent, and therefore are not power laws. In practice, however, observations often resolve small ranges of floe size, with the FSD fit to a straight lines in log-log space over that size range. We mimic this observational approach by naively

assuming that the distribution is fit to a power law slope in each size regime, with a coefficient either obtained by a least-squares fit or via equation (4), to demonstrate what might lead to differing interpretations of FSD slope and behavior at different length scales. The precise range of floe sizes in each regime is chosen based on the shape of the steady-state FSD. In applications to observations, the choice should be made on the basis of a statistical test for a power-law tail [Virkar and Clauset, 2014]. In the supporting Information Text S2 and Figure S3, we examine the sensitivity of the power-law decay coefficient α to the chosen width of these intervals.

The emergence of the distinct regimes (I) and (II) resembles observations in the Sea of Okhotsk and in East Antarctica, where at small scales the FSD was observed to decay with a shallower slope than at larger scales [Toyota *et al.*, 2006, 2011], with a transition occurring between 100 and 200 m. In each floe scale regime, we compute and plot the exponent of a power-law fit to the simulated FSD as solid lines in Figure 6d. We compare this result to the value of α obtained via equation (4). Now, r_1 and r_2 are the endpoints of the floe length scales considered in each regime (Figure 6d, dashed lines), and the variables c and P refer to the ice concentration and floe perimeter per square meter belonging to floes with size between r_1 and r_2 as discussed in section 2.2. To evaluate what terms in the FSD equation dominate at steady state, we compare the tendencies from each process in Figure 6e, averaged over the final 14 model days.

The first regime (I) of floe sizes, from 5 to 50 m, has a shallower slope than the incoming pack ice distribution (green dashed line, Figure 6b), decaying as a power law with an exponent -1 (Figure 6d, green solid line). This power law decay is consistent with observations of the FSD from small floes in a variety of contexts, in the Sea of Okhotsk [Inoue, 2004], the Arctic [Perovich and Jones, 2014], and the Antarctic [Toyota *et al.*, 2011]. At this scale, the main sink of ice area comes from mechanical interactions (Figure 6e, green line) as these floes, which constitute a majority of the ice area, frequently collide and consolidate to form larger and thicker ice floes. The influence of ice thermodynamics on the FSD is dominated by other processes (Figure 6e, blue line), but is most significant at the smallest floe sizes. At the smallest floe scales (5–20 m), the source of new ice area due to advection (Figure 6e, red line) balances a sink of ice area due to collisions. From 20 m to 50 m, a balance emerges between the source of area due to the fracture of larger ice floes by waves (Figure 6e, purple line) and the sink of area due to floe collisions.

The FSD slope in regime I is not captured by equation (4), which predicts a slope $\alpha=1.6$, closer to the slope of the pack ice FSD ($\alpha=2$) than to the slope of the FSD itself ($\alpha=0.9$). For comparison, the total floe perimeter per square kilometer area for two FSDs with slopes of $\alpha=0.9$ and $\alpha=1.6$, is roughly 105 and 240 km/km², correspondingly. In parameterization of lateral melt in climate models this would correspond to an increased lateral melt rate by a factor of about 250%. This discrepancy between the predicted and simulated power laws is due to a combination of the two factors discussed previously, the influence of ice thermodynamics at small floe sizes discussed in section 3.2, and the cutoff-error discussed in section 3.4.

In the second regime (II) covering floe sizes 50–150 m, floes are large enough to be fractured by the waves impinging on the model domain. The steady-state balance at this scale is between the influx of new ice area due to collisions between smaller floes in regime I, and the removal of ice area as floes are fractured by waves. This regime has a steep spectral slope which approaches $\alpha=6$ over time. In this range, the prediction of equation (4) is accurate. This change in power law slope resembles the “regime shift” identified by Toyota *et al.* [2006, 2011], whose scale has been hypothesized to be related to the flexural strength of small ice floes, but here is set by the peak wavelength of the ocean surface wave spectrum.

In the third regime (III), comprising floe sizes 150–1500 m, the most significant source of new ice area is advection of floes from the pack ice (Figure 6e, red line). The aspect ratio of these floes is small, and thermodynamic melting therefore does not significantly influence the evolution of the FSD at this scale. As floes belonging to regime III are larger than the peak wavelength of the ocean wave spectrum, all floes in regime III are readily fractured by the wave field, and the tendency due to wave fracture is therefore uniform as a function of r at this scale. As a result, the slope of the FSD in this regime is set by the slope of the ice being advected into the domain, $\alpha=2$ (Figure 6d, green lines). As this is the highest end of floe sizes considered in this simulation, there is no high-range cutoff, and the prediction made by equation (4) mirrors the simulated slope (Figure 6d, dashed green line).

Figure 6c shows the ice thickness distribution at several times during the simulation. Initially strongly peaked around $h=1$ m, the ITD is spread both into smaller and larger thicknesses by the external forcing.

Figure 6f shows the contribution to the steady-state balance from each individual forcing term. As wave fracture does not influence floe thicknesses, it does not lead to an ITD tendency. Advection from the pack ice (Figure 6f, red line) reinforces the Gaussian shape of the distribution by advecting ice floes with thicknesses near the peak of 1 m. Sea ice melting (Figure 6f, blue line) thins ice, shifting ice area from the peak thickness to smaller thicknesses. As the influence of lateral melting is generally small (see earlier discussion, Figure 6e, blue line), the total change in area due to the thermodynamic process is nearly zero. Mechanical collisions (Figure 6f, green line) do not conserve area, and move thinner ice to form thicker ice with reduced area, spreading the distribution to larger thicknesses.

4. Conclusions

We have simulated the evolution of the joint floe size and thickness distribution (FSTD), coupled to a mixed-layer ocean model, to understand the evolution of scaling laws in, the floe size distribution (FSD). The model simulates the FSTD evolution subject to different forcing factors: advection of sea ice into and out of the model domain, thermodynamic forcing from the ocean and atmosphere, mechanical interactions between colliding floes, and floe fracture due to ocean surface waves. We explored the response of the FSTD to each of the forcing factors, and to all of them combined, to gain a deeper understanding of how the scaling behavior of the FSD may evolve.

We note that the time evolution of mean quantities derived from the FSTD, such as the mean floe size and thickness, may evolve in a seemingly nonintuitive manner. Specifically, the time-dependence of these mean quantities may be different from that of the FSTD itself. This distinction could be important when interpreting observations and model simulations of the FSTD, and parameterizing its effects in models that do not resolve floe evolution in the detail considered here.

Next, we carefully examined the limitations of assuming a power law behavior by comparing two methods for computing power-law decay, one based on a least squares fit to the modeled FSD, and an observational technique that computes the floe size power law from observations of sea ice concentration and floe perimeter [Perovich and Jones, 2014]. We find two main sources of error can arise when using this simple observational method alone. The first source of error comes from when power-law scaling does not exist, or transient FSD evolution leads to a departure from scale-invariance. All of the forcing scenarios considered here exhibit at least some departure from scale-invariance. A second source of error arises due to an insufficiently large range of resolved floe sizes. This can lead to a bias even when the FSD is a power law with known slope. The two sources of error can lead to significant mis-estimations (>100%) of important metrics derived from the FSTD, such as the floe perimeter per unit area and mean floe size, which determine interactions between the FSTD and climate.

In addition to examining the constraints on calculating power laws of the FSD from observations, we also examined when such power laws are expected to arise and what physical balances may be responsible for their occurrence. We find that an initial power-law FSD will remain a power law if lateral melting is weak relative to basal melting. Under standard parameterizations of the effect of melting on ice floes [Steele, 1992] this is expected to be the case at floe sizes larger than a few tens of meters. However, Horvat *et al.* [2016] showed that when the effect of ocean eddies is considered, lateral melting is important even at large floe sizes, making power laws much less likely. We also show that the FSD also may deviate from a power law due to mechanical interactions when the sea ice is subjected to transient rather than steady forcing, and when floes are broken by ocean surface waves into a range of floe sizes.

By considering how multiple different forcing fields acting on different scales shape the FSD, we demonstrated the emergence of different behavior at different length scales, dividing the FSD into three distinct size regimes depending on the physical process that dominantly affects floes of each size range. For floes smaller than about 200 m, we find two separate regimes. The first, for sizes 5–50 m, is a shallow power law regime whose slope is set by the balance of ice advected into the domain, the fracture of larger floes, and the loss of ice area due to the floe collisions and merging. The second power law regime, for sizes 50–150 m, is a steeper power law regime that is determined by the balance of new floes formed through the collisions and merging of smaller floes balanced by the fracture by ocean surface waves. These two regimes combine to form a “joined power law” distribution similar to observations in the Antarctic [Toyota *et al.*, 2011]. The point (“regime shift”) at which the transition between the two subregimes occurs was not well understood previously, and was hypothesized to be related to the fragmentation of small ice floes. In our simulations we find that this can

be set by the ocean surface wave spectrum, which sets the typical size of fractured floes, however this does not rule out that fragmentation could determine the scale of floe breaking. More detailed observational studies of FSD evolution with and without the presence of ocean surface waves, should be done to determine in what forcing scenarios and in which size regime each fractural process is important.

The incorporation of sensitivity to floe size is an important aspect of modern sea ice modeling. Having details of the floe size evolution will provide useful information about the ice-ocean-atmospheric boundary layer, the rheology of the sea ice, the propagation of waves into and through the ice pack, the thermodynamic properties of the ice cover, and of mixing by wind, waves, and eddies in the ocean mixed layer. But it is important to achieve a careful understanding of how the combined FSTD evolves before incorporating or parameterizing its effects in climate studies, and to determine in which ways such an implementation can lead to biases in modeled sea ice evolution.

This study, therefore, is an intermediate step toward including the floe size distribution in climate models, and provides three lessons relevant to such models and to related observational analysis. First, we find (section 3.1) that the mean floe size and mean thickness cannot be assumed to advect and mix like passive tracer. This is because the mean flow thickness, for example, is the ratio of ice volume per unit area and ice concentration. These two quantities are conserved when mixed between two GCM grid cells, but their ratio, being a nonlinear function of the two, does not. Simple FSD models that represent only, say, the mean floe size [e.g., Williams et al., 2013], must take this into account. This can be accomplished by considering the relationship between mean floe size, the number of floes per unit area, and the ice concentration, or by evolving the FSD on its own. Second, it is difficult to justify using a single power law for representing the FSD, because of the different processes active at different scales (section 3.5, see also the observational analysis of Toyota et al. [2011]). In particular, because there is a known coupling between small floes and sea ice melting [Steele, 1992; Horvat et al., 2016], representing the different FSD dynamics at small scales (300 m and smaller) versus large scales is important. Additional observations of FSD evolution as function of scale are therefore also badly needed. Third, rigorous tools for testing whether the FSD decays as a power law should be applied to observations [Virkar and Clauset, 2014]. As demonstrated here, simpler methods might inadvertently lead to biases in estimated power laws.

In this study we provide insights into the different scale-selective physical processes acting on floes. We also demonstrate when assuming scaling behavior in observational analysis might be biased or incorrect. This added knowledge does not supplant the need for observations of the state and evolution of the FSTD/FSD and the relationship to these physical processes. How to make repeated observations of small-scale features such as the FSD (but also melt ponds, ridge distributions, and other subgrids cale sea ice features), in order to test appropriate process models for the next generation of global climate models, remains an important problem.

Appendix A: Time Stepping Scheme of FSTD Model

Floe categories must be represented by nonnegative areas, and the total ice concentration can never exceed one. Given an FSTD and a set of external forcing fields, these constraints place a strict bound on the model time-step in the forward Euler scheme described by equation (1). However, given the nonlinear relationship between the forcing and the FSTD, a model time-step that ensures these constraints are met is difficult to estimate, and may be smaller than necessary for numerical stability. To address this issue, we designed an adaptive time-stepping procedure which shortens the model time-step as needed. The positive definite constraint is that for all j, k ,

$$0 \leq f_{jk} \Delta A_{jk} \leq 1,$$

where $\Delta A_{jk} = \Delta r_j \Delta h_k$. In order to assure the positivity of the FSD, after computing the tendency in f_{jk} , for all $\{j, k\}$, the model time step $\Delta t = t^{i+1} - t^i$ is required to satisfy

$$\Delta t < \frac{f_{jk}}{\Delta f_{jk}},$$

where f_{jk} represent the value before the update during the current time step, and the delta term is the update value. Simultaneously, in order for the solution to be bounded by 1, the model time-step must satisfy the following for all $\{j, k\}$,

$$\Delta t < \frac{1 - f_{jk} \Delta A_{jk}}{\Delta f_{jk} \Delta A_{jk}}.$$

The updated model time-step Δt is then chosen as the maximum value for which all constraints are met and $\Delta t \leq \Delta t_0$, where Δt_0 is a global time-step specified at the beginning of the simulation. The external forcing fields (wave spectrum, heating) are updated every Δt_0 . The matrix \mathbf{f} is updated using the time step Δt , and the procedure is then repeated using an initial step of $\Delta t_0 - \Delta t$, reducing it as necessary, until the next update of the external forcing fields after a time Δt_0 elapsed. At that point the time stepping is reinitialized with $\Delta t = \Delta t_0$.

Appendix B: Mixed-Layer Model

The ocean mixed layer model closely follows *Petty et al.* [2013] in that it is composed of a mixed-layer ocean and surface layer, but it has been adapted to fit within the FSTD framework of *Horvat and Tziperman* [2015]. Below we demonstrate how the temperatures and salinities of the ice, surface layer, and mixed layer are determined. For further discussion of the properties of these models, see *Petty et al.* [2013] and *Tsamados et al.* [2015].

B1. Ice Surface Temperature

The ice surface temperature, $T_{s,i}$, is calculated via a balance of the fluxes of sensible cooling, latent cooling and longwave emission, longwave absorption, shortwave absorption, and conductive heating at the ice surface,

$$\begin{aligned} Q_{surf}(T_{s,i}) = & \rho_a c_a C_D^i U_a (T_{s,i} - T_a) + \\ & + \rho_a L_s C_D^i U_a (q_{sat}(T_{s,i}, P) - q_a) + \epsilon_i \sigma T_{s,i}^4 \\ & - \epsilon_i Q_{LW} - (1 - \alpha_i) Q_{SW} - Q_c(T_{s,i}) = 0, \end{aligned} \quad (B1)$$

where ρ_a is the atmospheric density, c_a is its specific heat capacity, C_D^i is the turbulent heat transfer coefficient over ice, U_a is the 10 m wind, T_a 10 m atmospheric temperature, L_s is the latent heat of sublimation, $q_{sat}(T_{s,i})$ is the saturation specific humidity at temperature $T_{s,i}$ and atmospheric pressure P , q_a is the atmospheric specific humidity, ϵ_i is the emissivity of sea ice, Q_{LW} is the downwelling long-wave heat flux, α_i is the albedo of sea ice, Q_{SW} is the downwelling short-wave heat flux, and Q_c is the conductive heat flux through the ice (positive upward). We assume that none of the downwelling shortwave radiation penetrates through the ice. The thermodynamic component of the HT model is configurable with any column thermodynamical model. For the presentation of these results, we use the simple 0-layer model of *Semtner* [1976]. The conductive heat flux is calculated by integrating the diffusion equation over the sea-ice layer, to give,

$$Q_c = \frac{\kappa_i (T_f - T_{s,i})}{h_i},$$

where κ_i is the conductivity of sea ice, and a positive Q_c has a warming effect on the surface. If the diagnosed sea-ice surface temperature is above the melting point, we set $T_{s,i} = 0^\circ \text{C}$ and we compute the residual heat flux from this temperature $Q_{surf}(0^\circ \text{C})$, which is used to melt the sea ice at its surface,

$$\frac{\partial h}{\partial t_{surf}} = \frac{Q_{surf}}{\rho_i L_f}.$$

B2. Ocean Surface Temperature

The ocean surface temperature $T_{s,o}$ is determined through another balance of turbulent and radiative heat fluxes with the atmosphere, with the mixed layer below and with the sea ice. The total atmospheric heating of the surface layer, $R(T_{s,o})$, is,

$$\begin{aligned} R(T_{s,o}) = & (1 - \alpha_w)(1 - l_0) Q_{SW} \\ & + \epsilon_o Q_{LW} \\ & - \rho_a c_a C_D^o U_a (T_{s,o} - T_a) \\ & - \rho_a L_v C_D^o U_a (q_{sat}(T_{s,o}, P) - q_a) \\ & - \epsilon_o \sigma T_{s,o}^4, \end{aligned} \quad (B2)$$

where C_D^o is the turbulent transfer coefficient above ocean, L_v is the latent heat of vaporization, and ϵ_o is the ocean emissivity. The surface layer absorbs some of the solar radiation, and we define l_0 to be the fraction

of the solar radiation arriving at the top of the mixed layer, so that $1 - I_0$ is the fraction absorbed in the surface layer. A positive R has a warming effect on the surface.

The surface layer also exchanges turbulent heat fluxes with the mixed layer below. We assume the turbulent exchange is proportional to a friction velocity $u^* = \sqrt{\tau/\rho_w}$, where τ is the wind stress. With the approximation that τ is proportional to the square of the wind velocity U_a , and a bulk momentum transfer coefficient, the friction velocity in a region of open water u_o^* , in a region under sea ice u_i^* , and averaged over the domain u^* are defined,

$$u_o^* = \sqrt{\frac{\tau_o}{\rho_w}} = U_a \sqrt{\frac{\rho_a C_D^o}{\rho_w}},$$

$$u_i^* = \sqrt{\frac{\tau_i}{\rho_w}} = U_a \sqrt{\frac{\rho_a C_D^i}{\rho_w}},$$

$$u^* = \sqrt{\frac{c\tau_i + (1-c)\tau_o}{\rho_w}} = U_a \sqrt{\frac{\rho_a}{\rho_w} (cC_D^i + (1-c)C_D^o)},$$

where c is the ice concentration. In a region of open water, the turbulent exchange between the surface layer and the mixed layer $Q_{mo}(T_{s,o})$ is,

$$Q_{mo}(T_{s,o}) = \rho_w c_w U_o^* (T_{mix} - T_{o,s}), \tag{B3}$$

where c_w is the specific heat capacity of seawater, and T_{mix} is the mixed-layer temperature. The net heat exchange per unit area is this factor multiplied by the open water fraction, ϕ .

The shallow surface layer exchanges heat laterally with the "lead" region. The number of floes per unit area, per floe size, is denoted $N(\mathbf{r}) = f(\mathbf{r})(\pi r^2)^{-1}$. For a circular floe of size $\mathbf{r} = (r, h)$, the lateral surface area of its boundary layer is $2\pi(r+r_{lw})(h+0.1\text{m})$. The total area shared between the ocean surface region and the boundary layer per unit area, A_{side} is therefore computed via the FSTD as,

$$A_{side} = 2\pi \int_{\mathbf{r}} N(\mathbf{r})(r+r_{lw})h \, d\mathbf{r}.$$

This factor increases when the number of floes per unit area is larger (i.e., the mean floe size is smaller), as the floes have a greater surface area. The turbulent exchange per unit area shared between the ocean surface layer and sea ice lateral boundary layer, $Q_{si}(T_{s,o})$, is computed as,

$$Q_{si}(T_{s,o}) = \rho_w c_w c_h U_o^* (T_f - T_{o,s}).$$

The magnitude of the turbulent flux is reduced by a factor c_h , a Stanton number, that describes the weakening of the turbulent exchange near the solid ice boundary [McPhee, 1992]. For a 1 degree temperature difference and a 1 cm/s friction velocity, the heat flux is approximately 200 W/m² [Pollard et al., 1983; Tang, 1991]. The net heat exchange (per unit area) is therefore $A_{side} Q_{si}$.

We determine the ocean surface temperature $T_{s,o}$ using an energy balance for the surface layer,

$$\phi(R(T_{s,o}) + Q_{mo}(T_{s,o})) + A_{side} Q_{si}(T_{s,o}) = 0,$$

which initially assumes that there is no latent heat release due to sea-ice growth. Fluxes that occur in regions of open water are multiplied by the open water fraction ϕ , where $\phi = 1 - c$, for c the ice concentration. If the ocean surface temperature $T_{s,o}$ calculated using this balance is colder than the freezing point, new sea ice is formed. We then compute the same budget with $T_{s,o} = T_f$, and add the latent heat release due to sea ice formation at the ocean surface, Q_o . The residual heat loss is compensated for by latent heat released due to new sea-ice formation, i.e.,

$$Q_o = \phi(R(T_f) + Q_{mo}(T_f)), \tag{B4}$$

noting that $Q_{si}(T_f) = 0$.

B3. Ice Thermodynamics

In the FSTD model of Horvat and Tziperman [2015], the effect of ocean heating on sea ice is cast in terms of three heat fluxes: a heat flux to the base of floes, $Q_{l,b}$, a heat flux to the sides of floes, $Q_{l,l}$, and an open-water heat flux Q_o . The partitioning of ocean heating between the two is based on the aspect ratio of individual floes, as in Steele [1992]. The open-water heat flux is zero when the surface ocean temperature is reduced to its freezing point (equation (B4)). This method of computing ice heat fluxes is distinct from that which is present in modern sea ice models. For example, in melting, the Community Sea Ice model assumes all of the heating of the ocean surface layer can be used to melt sea ice. In contrast, the geometric sea-surface partitioning method of Horvat and Tziperman [2015] allows for the presence of warm ocean surface waters in regions away from floes, which is more realistic [Perovich, 2003].

The heat flux into the lead area, however, arises from both the turbulent exchange with the surface layer, $Q_{s,l}$, and the turbulent exchange between the mixed layer and the ice base. The heat exchanged between the mixed layer and ice base is,

$$Q_{mi} = \rho_w c_w c_h u_i^* (T_{mix} - T_f), \quad (B5)$$

where the ice is at its freezing point at its base. The lead heat flux, Q_{lead} , which affects the development of floes, is the sum of the lateral exchange between the floe boundary layer and the ocean surface layer and the turbulent exchange between the ice base and the ocean mixed layer,

$$Q_{lead} = A_{side} Q_{si} + c Q_{mi}.$$

The time rate of change of ice thickness $G_h(h)$, depends on the basal component of the lead heat flux, $Q_{l,b}$, the conductive heat flux going from the ice base to the ice surface $Q_c(T_{s,i})$, and the surface heat flux $Q_{surf}(T_{s,i})$. Adding the three together, we obtain the time rate of change of ice thickness,

$$G_h = \frac{Q_{surf}(T_{s,i}, h)}{\rho_i L_f} + \frac{Q_c(T_{s,i}) - Q_{l,b}}{0.9 \rho_i L_f},$$

where the value of 0.9 multiplying the enthalpy of fresh ice $\rho_i L_f$ accounts for the increased salinity at the ice base, and we assume the surface ice is fresh [Bitz and Lipscomb, 1999]. The part of the lead heat flux that causes lateral melting is used to melt sea ice in contact with sea-water, so that the time rate of change of floe size, G_r is,

$$G_r = \frac{Q_{l,l}}{0.9 \rho_i L_f}.$$

B4. Mixed Layer

The mixed layer temperature T_{ml} and salinity S_{ml} are calculated as function of time, and its depth H_{ml} is prescribed and, for simplicity, constant in our simulations. The mixed layer exchanges heat and salt with a resting deep layer. In this study we prescribe a constant temperature and salinity equal to the initial mixed-layer temperature and salinity, $T_d = -1.8^\circ \text{C}$, $S_d = 33 \text{ PSU}$. Assuming a coefficient of vertical eddy diffusivity κ , the turbulent exchange of temperature between the mixed layer and deep layer is,

$$Q_{dm} = \rho c_w \kappa \frac{T_d - T_{ml}}{H_{ml}} = \rho c_w \kappa \frac{\Delta T_d}{H_{ml}}.$$

The mixed layer is also influenced by solar radiation penetrating through the surface layer, and via the exchange of heat between it and the surface layer and ice. The net heat flux within the mixed layer by penetrating shortwave or surface exchange, Q_{ml} , is,

$$\begin{aligned} Q_{ml} = & \phi \cdot (1 - \alpha_w) I_0 (1 - e^{-\kappa_w H_{ml}}) Q_{SW} \\ & - \phi \cdot Q_{mo}(T_{s,o}) \\ & + c \cdot Q_{mi}(T_{mix}). \end{aligned} \quad (B6)$$

Positive Q_{ml} means mixed-layer warming. There are three components to Q_{ml} . The first is the absorption of shortwave radiation. A fraction I_0 of the solar radiation incident over water, ϕQ_{SW} , passes through the surface layer. A fraction $(1 - e^{-\kappa_w H_{ml}})$ of this, where κ_w is the extinction coefficient of shortwave radiation in

seawater, is absorbed in the mixed layer. The second term, ϕQ_{mo} , is the heat exchanged with the ocean surface layer, and the third term, $c \cdot Q_{mi}$, is the heat exchanged with the ice.

The net salt flux into the mixed layer from above per unit area, F_S (in psu m/s), is,

$$F_S = \frac{\rho_i}{\rho_w} (S_{mix} - S_i) \frac{\partial V_i}{\partial t} - (P - E) S_{mix},$$

with positive Q_s implying that the mixed-layer becomes saltier. V_i is the ice volume per unit area, $(P - E)$ (in m/s) is the precipitation minus evaporation rate per unit area, and S_{mix} is the mixed layer salinity. The evaporation rate E is calculated from the latent heat fluxes in equations (B1) and (B2). The precipitation P is prescribed as the total precipitation reaching the ocean. F_S is therefore the sum of salinity tendency due to ice melting or freezing, and evaporation minus precipitation.

The full equations for determining the evolution of mixed layer temperature and salinity are, therefore,

$$\frac{\partial T_{ml}}{\partial t} = \frac{Q_{ml}}{\rho_w c_w H_{ml}} + \Delta T_d \left(\frac{\kappa}{H_{ml}^2} \right) \quad (B7)$$

$$\frac{\partial S_{ml}}{\partial t} = \frac{F_S}{H_{ml}} + \Delta S_d \left(\frac{\kappa}{H_{ml}^2} \right). \quad (B8)$$

Acknowledgments

We thank Michel Tsamados and two anonymous reviewers for their helpful feedback. This research was supported by NASA under grant NNX14AH39G and NSF Physical Oceanography program, grant OCE-1535800. CH was supported by the Department of Defense (DoD) through the National Defense Science & Engineering Graduate Fellowship (NDSEG) Program. ET thanks the Weizmann institute for its hospitality during parts of this work. CH thanks the Butler Conservation Fund for their hospitality during parts of this work. We thank Radha Mastandrea for helping to test the model code. No new data sets were generated during the production of this work. Model results are publicly available at <http://www.seas.harvard.edu/climate/eli/Downloads/Sea-ice-floe-size-distribution/>.

References

- Bennetts, L. G., and T. D. Williams (2014), Water wave transmission by an array of floating discs, *Philos. Trans. R. Soc. A*, 471(2173), 2,014,0698–2,014,0698, doi:10.1098/rspa.2014.0698.
- Birnbaum, G., and C. Lüpkes (2002), A new parameterization of surface drag in the marginal sea ice zone, *Tellus, Ser. A*, 54(1), 107–123, doi:10.1034/j.1600-0870.2002.00243.x.
- Bitz, C. M. (2008), Numerical modeling of sea ice in the climate system, technical report, Univ. of Wash., Seattle, Wash. [Available at http://www.atmos.uw.edu/~bitz/Bitz_chapter.pdf].
- Bitz, C. M., and W. H. Lipscomb (1999), An energy-conserving thermodynamic model of sea ice, *J. Geophys. Res.*, 104(C7), 15,669–15,677, doi:10.1029/1999JC900100.
- Clauset, A., C. Rohilla Shalizi, and M. E. J. Newman (2009), Power-law distributions in empirical data, *SIAM Rev.*, 51(4), 661–703, doi:10.1214/13-AOS710.
- Dumont, D., A. Kohout, and L. Bertino (2011), A wave-based model for the marginal ice zone including a floe breaking parameterization, *J. Geophys. Res.*, 116, C04001, doi:10.1029/2010JC006682.
- Feltham, D. L. (2008), Sea ice rheology, *Annu. Rev. Fluid Mech.*, 40(1), 91–112, doi:10.1146/annurev.fluid.40.111406.102151.
- Herman, A. (2011), Molecular-dynamics simulation of clustering processes in sea-ice floes, *Phys. Rev. E*, 84, 1–11, doi:10.1103/PhysRevE.84.056104.
- Herman, A. (2012), Influence of ice concentration and floe-size distribution on cluster formation in sea ice floes, *Cent. Eur. J. Phys.*, 10, 715–722, doi:10.2478/s11534-012-0071-6.
- Horvat, C., and E. Tziperman (2015), A prognostic model of the sea-ice floe size and thickness distribution, *Cryosphere*, 9(6), 2119–2134, doi:10.5194/tc-9-2119-2015.
- Horvat, C., E. Tziperman, and J.-M. Campin (2016), Interaction of sea ice floe size, ocean eddies, and sea ice melting, *Geophys. Res. Lett.*, 43, 8083–8090, doi:10.1002/2016GL069742.
- Inoue, J. (2004), Ice floe distribution in the Sea of Okhotsk in the period when sea-ice extent is advancing, *Geophys. Res. Lett.*, 31, L20303, doi:10.1029/2004GL020809.
- Joyce, J. M. (2011), *Kullback-Leibler Divergence*, pp. 720–722, Springer, Berlin, doi:10.1007/978-3-642-04898-2.
- Kanamitsu, M., W. Ebisuzaki, J. Woollen, S.-K. Yang, J. J. Hnilo, M. Fiorino, and G. L. Potter (2002), NCEP-DOE AMIP-II Reanalysis (R-2), *Bull. Am. Meteorol. Soc.*, 83(11), 1631–1643, doi:10.1175/BAMS-83-11-1631(2002)083(1631:NAR)2.3.CO;2.
- McPhee, M. G. (1992), Turbulent heat flux in the upper ocean under sea ice, *J. Geophys. Res.*, 97(C4), 5365–5379, doi:10.1029/92JC00239.
- Michel, W. H. (1999), Sea spectra revisited, *Mar. Technol.*, 36(4), 211–227.
- Perovich, D. K. (2003), Thin and thinner: Sea ice mass balance measurements during SHEBA, *J. Geophys. Res.*, 108(C3), 8050, doi:10.1029/2001JC001079.
- Perovich, D. K., and K. F. Jones (2014), The seasonal evolution of sea ice floe size distribution, *J. Geophys. Res. Oceans*, 119, 8767–8777, doi:10.1002/2014JC010136.
- Petty, A. A., D. L. Feltham, and P. R. Holland (2013), Impact of atmospheric forcing on Antarctic continental shelf water masses, *J. Phys. Oceanogr.*, 43(5), 920–940, doi:10.1175/JPO-D-12-0172.1.
- Petty, A. A., P. R. Holland, and D. L. Feltham (2014), Sea ice and the ocean mixed layer over the Antarctic shelf seas, *Cryosphere*, 8(2), 761–783, doi:10.5194/tc-8-761-2014.
- Pollard, D., M. L. Batten, and Y.-J. Han (1983), Development of a simple upper-ocean and sea-ice model, *J. Phys. Oceanogr.*, 13(5), 754–768, doi:10.1175/1520-0485(1983)013<0754:DOASUO>2.0.CO;2.
- Rynders, S., Y. Aksenov, D. Feltham, G. Nurser, and A. Naveira Garabato (2016), Modelling MIZ dynamics in a global model, in *EGU General Assembly Conference Abstracts*, vol. 18, 1004 pp.
- Schulson, E. M. (2004), Compressive shear faults within arctic sea ice: Fracture on scales large and small, *J. Geophys. Res.*, 109, C07016, doi:10.1029/2003JC002108.
- Semtner, A. J. (1976), A model for the thermodynamic growth of sea ice in numerical investigations of climate, *J. Phys. Oceanogr.*, 6(3), 379–389, doi:10.1175/1520-0485(1976)006<0379:AMFTTG>2.0.CO;2.
- Steele, M. (1992), Sea ice melting and floe geometry in a simple ice-ocean model, *J. Geophys. Res. Oceans*, 97(C11), 17,729–17,738, doi:10.1029/92JC01755.

- Steer, A., A. Worby, and P. Heil (2008), Observed changes in sea-ice floe size distribution during early summer in the western Weddell Sea, *Deep Sea Res., Part II*, 55(8–9), 933–942, doi:10.1016/j.dsr2.2007.12.016.
- Tang, C. L. (1991), A two-dimensional thermodynamic model for sea ice advance and retreat in the Newfoundland marginal ice zone, *J. Geophys. Res.*, 96(C3), 4723–4737, doi:10.1029/90JC02579.
- Thorndike, A. S., D. A. Rothrock, G. A. Maykut, and R. Colony (1975), The thickness distribution of sea ice, *J. Geophys. Res.*, 80(33), 4501–4513, doi:10.1029/JC080i033p04501.
- Toyota, T., S. Takatsuji, and M. Nakayama (2006), Characteristics of sea ice floe size distribution in the seasonal ice zone, *Geophys. Res. Lett.*, 33, L02616, doi:10.1029/2005GL024556.
- Toyota, T., C. Haas, and T. Tamura (2011), Size distribution and shape properties of relatively small sea-ice floes in the Antarctic marginal ice zone in late winter, *Deep Sea Res., Part II*, 58(9–10), 1182–1193, doi:10.1016/j.dsr2.2010.10.034.
- Tsamados, M., D. L. Feltham, D. Schroeder, D. Flocco, S. L. Farrell, N. Kurtz, S. W. Laxon, and S. Bacon (2014), Impact of variable atmospheric and oceanic form drag on simulations of Arctic Sea ice, *J. Phys. Oceanogr.*, 44(5), 1329–1353, doi:10.1175/JPO-D-13-0215.1.
- Tsamados, M., D. Feltham, A. Petty, D. Schroeder, and D. Flocco (2015), Processes controlling surface, bottom and lateral melt of Arctic sea ice in a state of the art sea ice model, *Philos. Trans. R. Soc. A*, 17, 10,302, doi:10.1098/rsta.2014.0167.
- Virkar, Y., and A. Clauset (2014), Power-law distributions in binned empirical data, *Ann. Appl. Stat.*, 8(1), 89–119, doi:10.1214/13-AOAS710.
- Williams, T. D., L. G. Bennetts, V. a. Squire, D. Dumont, and L. Bertino (2013), Waveice interactions in the marginal ice zone. Part 1: Theoretical foundations, *Ocean Modell.*, 71, 81–91, doi:10.1016/j.ocemod.2013.05.010.
- Zhang, J., A. Schweiger, M. Steele, and H. Stern (2015), Sea ice floe size distribution in the marginal ice zone: Theory and numerical experiments, *J. Geophys. Res. Oceans*, 120, 3484–3498, doi:10.1002/2015JC010770.
- Zhang, J., H. Stern, B. Hwang, A. Schweiger, M. Steele, M. Stark, and H. C. Graber (2016), Modeling the seasonal evolution of the Arctic sea ice floe size distribution, *Elementa*, 4, 000126, doi:10.12952/journal.elementa.000126.